

Polarization Diversity and Transfer Learning-Based Modulation Optimization for High-Speed Dual Channel MIMO Backscatter Communication

Hyunmin Jeong¹, Nohgyeom Ha¹, Apostolos Georgiadis², *Fellow, IEEE*, Manos M. Tentzeris², *Fellow, IEEE*, and Sangkil Kim¹, *Senior Member, IEEE*

Abstract—This article presents a novel approach to address the challenges in backscatter communication (BackCom) for the Internet of Things. The traditional use of I/Q load modulator based on parametric transistor models often suffers from performance degradation due to discrepancies with actual transistor models caused by thermal and environmental noise sources. To overcome this issue, this article proposes an active circuit modeling technique based on artificial neural network (ANN)-based transfer learning, which utilizes actual measurement data to model the I/Q load modulator accurately. Furthermore, an optimization algorithm is applied to achieve an optimal high-order modulation scheme, leading to improved energy efficiency by 40%. By leveraging machine learning-based modeled I/Q modulators, the proposed approach enables high-speed wireless data communication in a dual-channel configuration. This article also conducts theoretical analysis to define the required performance of a dual-polarized Vivaldi antenna for implementing polarization diversity in BackCom. This analysis provides guidelines for achieving optimal performance in terms of spectral efficiency and error vector magnitude (EVM). The experimental results demonstrate that the proposed approach achieves a spectral efficiency of 2.0 bps/Hz based on 4-QAM modulation within a 150-MHz bandwidth. The measured EVM is 9.35%, indicating the effectiveness of the proposed technique in achieving reliable and efficient wireless data communication in backscatter systems. This article presents a comprehensive approach combining accurate circuit modeling, optimization algorithms, and theoretical analysis to enable high-speed, ultralow-power wireless data communication in BackCom systems.

Index Terms—Artificial neural network (ANN), backscatter communication (BackCom), dual-polarized antenna, Internet of Things (IoT), k -nearest neighbor (k -NN), machine learning, multiple-input-multiple-output (MIMO), polarization diversity, transfer learning, Vivaldi antenna.

I. INTRODUCTION

THE Internet of Things (IoT) is a transformative technology that connects everyday objects and systems to enable communication and data sharing. It has the potential to

Manuscript received 14 July 2023; revised 10 November 2023, 26 December 2023, and 14 February 2024; accepted 10 March 2024. Date of publication 20 March 2024; date of current version 7 June 2024. This work was supported by the National Research Foundation of Korea (NRF) Grant funded by the Korea Government (MSIT) under Grant RS-2023-00237172. (*Corresponding author: Sangkil Kim.*)

Hyunmin Jeong, Nohgyeom Ha, and Sangkil Kim are with the Department of Electronics Engineering, Pusan National University, Busan 46241, Republic of Korea (e-mail: ksangkil3@pusan.ac.kr).

Apostolos Georgiadis resides in 2582 CN The Hague, The Netherlands.

Manos M. Tentzeris is with the School of Electrical and Computer Engineering, Georgia Institute of Technology, Atlanta, GA 30318 USA.

Digital Object Identifier 10.1109/JIOT.2024.3379854

revolutionize various industries, but it also presents challenges in terms of self-sustainability, power-consumption, and high-speed wireless communication.

Backscatter communication (BackCom) has emerged as an energy-efficient and low-power wireless data communication method that addresses those challenges [1], [2], [3], [4], [5], [6].

BackCom involves changing the load impedance to reflect the surrounding environment or incident waves, enabling communication with minimal active devices. It can be categorized into digital modulation and analog modulation [7]. Digital modulation involves using a microcontroller unit (MCU) or field-programmable gate array (FPGA) to select a fixed load impedance for modulation, offering high accuracy but higher power consumption and limited modulation freedom [8], [9], [10]. In contrast, analog modulation utilizes analog circuits with components like pin diode or field effect transistor (FET), providing lower power consumption and greater modulation flexibility. While analog modulation may have lower accuracy, it has garnered significant attention due to its advantages in terms of power efficiency and modulation freedom. Recent studies have focused on exploring the potential of analog modulation in various applications [11], [12], [13], [14]. Ultimately, the choice between digital and analog modulation depends on the specific requirements of the application, considering factors, such as accuracy, power consumption, and modulation flexibility.

Traditional BackCom studies have primarily utilized simple modulation schemes like amplitude shift keying (ASK) and binary phase shift keying (BPSK), which have limited data rates. To overcome this limitation, higher order modulation schemes like quadrature amplitude modulation (QAM) have been introduced. However, selecting the optimal QAM modulation scheme to achieve low-bit error rate (BER) and high-data rates is challenging due to the complexity of analog modulation.

There are two key challenges in BackCom: 1) accurate modeling of the load modulator and 2) selection of the optimal QAM scheme based on a load modulator model to minimize the BER and achieve high-data rates. Modeling the load modulator's environment is challenging due to discrepancies between simulations and measurements, making it difficult to determine the optimal reflection coefficient. The optimal QAM modulation scheme needs to be selected based on modeled reflection coefficients to achieve low-BER and high-data rates.

These challenges require careful analysis and consideration to ensure optimal performance and efficient data communication in backscatter systems.

The existence of a precisely modeled reflection coefficient facilitates the implementation of optimal QAM in BackCom, thereby enabling the utilization of various wireless communication techniques. This success builds upon the achievements observed in conventional wireless channels. First of all, it is apparent that channel estimation errors shows variability based on the composition of the training matrix [15]. Consequently, this provides the opportunity to construct an optimal training matrix, incorporating modeled reflection coefficients.

Second, considering that a standard backscatter channel functions as a two-way channel, the challenge of fading assumes greater complexity compared to conventional wireless channels. Therefore, dedicated endeavors have been made to integrate orthogonal space-time coding (OSTBC) into backscattered tags using various techniques [16], [17]. These efforts aim to enhance reliability in BackCom through the adoption of multiple-input–multiple-output (MIMO) communication. To ensure the effective deployment of OSTBC, maintaining orthogonality between symbols is crucial. In this regard, optimizing coding based on modeled reflection coefficients holds significant importance. To effectively integrate polarization diversity, a crucial MIMO technique, it is critical to calculate the modulation factor between symbols and engineer antennas optimized to attain the required cross-polarization suppression level, ensuring orthogonal polarization between antennas. The comprehensive modeling of reflection coefficients thus represents a highly significant contribution to the field of ultralow power communications, including BackCom.

A. Related Work

Previous research efforts on MIMO BackCom systems have demonstrated and proposed numerous approaches and ideas. The initial investigation of the multiantenna tag channel was introduced in [18]. Subsequent extensions of this research primarily focused on the uncoded BER for the multiple-input–single-output (MISO) channel [19]. Studies featuring multiple backscattering tag antennas and diversity orders were presented in [16] and [20]. Additionally, He et al. [21] contributed to the enhancement of BackCom’s practicality by theoretically affirming the effectiveness of a simple yet high-performance space-time code within the context of $2 \times 2 \times 2$ MIMO BackCom system.

Research efforts on integrating nonorthogonal multiple access (NOMA) into BackCom are reported in [22], [23], and [24]. These efforts concentrate on improving spectral and energy efficiency, as well as multiplexing capabilities. The primary strategy in these approaches involves the use of resilient power control, which operates simultaneously on the same frequency. However, these papers are constrained by their reliance on simulations and theoretical analyses, lacking incorporation of actual measurement data. Several research endeavors have emphasized the implementation of parallel decoding, utilizing empirical measurements with multiple tags to enhance throughput via

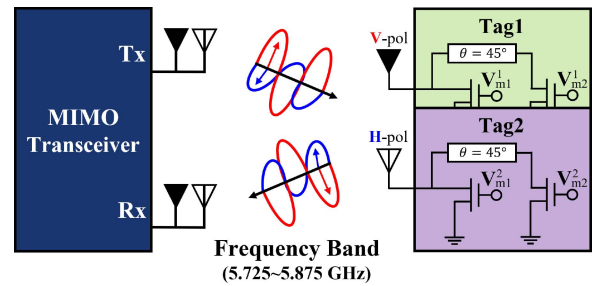


Fig. 1. Proposed MIMO BackCom system.

the wireless identification and sensing platform (WISP) [25], [26], [27], [28]. However, It is crucial to note that these works provide an incomplete illustration of MIMO BackCom, as they lack consideration of multiplexing in the transceiver. This article introduces the application of polarization diversity through the integration of MIMO technology with multiple tags and multiple transceivers for BackCom, alongside the comprehensive modeling of the reflection coefficients of I/Q load modulators, marking a pioneering contribution in this domain.

B. Contribution and Novelty

This article introduces a method for modeling I/Q load modulators using transfer learning. This approach enables precise modeling of reflection coefficients and the implementation of higher order QAM schemes based on the proposed optimization algorithm. Furthermore, this article presents $2 \times 2 \times 2$ MIMO BackCom systems and demonstrates the application of polarization diversity through theoretical analysis and measurements in over-the-air (OTA) environments, effectively doubling the spectral efficiency within a designated bandwidth (BW) in Fig. 1. These advancements have significantly contributed to the practical implementation of MIMO BackCom and IoT communications. The proposed algorithm and MIMO BackCom are evaluated within the C-band of the industrial, scientific, and medical (ISM) band, ranging from 5.725 to 5.875 GHz (BW = 150 MHz).

This article is organized as follows. Section II involves the theoretical verification of polarization diversity in MIMO BackCom, and Section III presents a modeling approach for the I/Q load modulator and an algorithm for selecting the optimal QAM modulation method. The design of RF front-end system to validate polarization diversity and the proposed optimization algorithms is discussed in Section IV. Antenna design and measurement procedures for implementing polarization diversity are elaborated in Sections V and VI. The theory of polarization diversity and the optimal QAM modulation method are verified through OTA measurements in Section VII. This article concludes with a summary of findings in Section VIII.

II. MIMO BACKCOM SYSTEM DESIGN

The first step in implementing an optimized BackCom system based on the polarization diversity is to calculate the received power in a single-input–single-output (SISO) system.

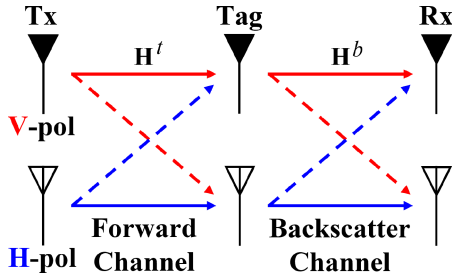


Fig. 2. BackCom channel with polarization diversity: $2 \times 2 \times 2$.

A. SISO BackCom Analysis

The calculation of the received power P_R in the BackCom system is shown in

$$P_R = \frac{P_T G_R G_T G_t^2 \lambda^4 X_f X_b M}{(4\pi)^4 r_f^2 r_b^2 \Theta^2 B_f B_b F} \quad (1)$$

where P_T is the transmit power of the transceiver [29]. G_R and G_T are the transmitter (Tx) and receiver (Rx) antenna gains of the transceiver, respectively. G_t is the antenna gain of a backscattering tag. λ is the frequency wavelength. X_f and X_b are the polarization mismatch in the forward and backward directions, respectively. $M \triangleq |\Gamma_A - \Gamma_B|^2/4$ represents the backscatter modulation factor. Γ_A and Γ_B are arbitrary reflection coefficients, and in BackCom, they have a given value by the I/Q load modulator. r_f and r_b are the distance between the transceiver and the tag, respectively. Θ is the tag's antenna gain degradation due to the environment. B_f and B_b are the blockage loss in the forward and backward directions. F is the backscatter link fade margin.

To simplify the system, it was assumed that there is no antenna gain degradation and that the same antennas are used, resulting in $G = G_R = G_T = G_t$ and $\Theta = 0$. In line-of-sight (LOS) communications, when there are no polarization mismatches, the blockage losses (B_f and B_b) can be considered negligible. In the BackCom system being considered, it is assumed to be quasi-monostatic, allowing for $r_f = r_b = r$ to be achieved. In an ideal situation without fading, the fading factor F is eliminated. The reformulated received backscattered power \bar{P}_R is shown in

$$\bar{P}_R = \frac{P_T G^4 \lambda^4 M}{(4\pi)^4 r^4}. \quad (2)$$

The simplified expression for \bar{P}_R is applicable for SISO systems. In the case of MIMO systems, the channel structure involving multiple antennas should be considered.

This work presents the application of the polarization diversity technique in the BackCom system to enhance the data rate. By utilizing an ideal antenna with distinct vertical polarization (V-pol) and horizontal polarization (H-pol) properties, as depicted in Fig. 2, the received power from each polarization remains unaffected by the presence of other polarizations, allowing (2) to be employed for the calculation of received power. However, it is important to note that real-world scenarios present challenges in designing antennas that perfectly conform to ideal specifications without any cross-polarization level. In practical antenna design and the BackCom system, it is essential to consider factors,

such as antenna structure, atmospheric effects, and multipath reflections, as they introduce cross-polarization components. These components should be regarded as noise sources and taken into account during system design and performance evaluation. Therefore, even in BackCom systems incorporating polarization diversity, it remains necessary to accurately model the received power, considering the realistic characteristics of the antennas and accounting for associated effects. By incorporating these realistic antenna characteristics and effects into the system modeling, a more comprehensive understanding of the system's performance can be achieved, enabling better optimization and evaluation of the BackCom system.

B. MIMO BackCom Channel Analysis

In order to achieve maximum data rate in high-speed BackCom systems, it is crucial to maximize the desired co-polarization (Co-pol) component for each polarization while minimizing the unwanted cross-polarization (X-pol) component. However, there is a lack of reported research efforts on the application of polarization diversity and the appropriate level of X-pol suppression. This article aims to fill this gap by providing clear guidelines for X-pol suppression levels through an analytical analysis of N -QAM (4-, 16-, and 64-QAM) modulation schemes based on symbol boundaries. By examining the modulation schemes and analyzing the symbol boundaries, this study intends to determine the impact of different X-pol suppression levels on system performance.

The objective is to establish guidelines that can optimize the performance and data rate in high-speed BackCom systems. The findings from this research will contribute to the understanding of polarization diversity and its implementation in practical BackCom systems.

The analysis focuses on the impact of different levels of cross-polarization suppression on system performance, using the error vector magnitude (EVM). By evaluating these modulation schemes under varying degrees of X-pol suppression level, the requirements for achieving optimal performance can be determined. This analysis aims to provide insights into the performance characteristics and requirements for implementing polarization diversity in BackCom systems, ultimately contributing to the optimization of system performance and data rate. The analysis begins by expressing the received signal y obtained from the received power (\bar{P}_R) in the SISO channel as follows:

$$y = h^b \Gamma h^t x + L + w \quad (3)$$

where x is the signal transmitted from a transceiver. h^t and h^b are the forward and backscatter channels, respectively. L is a constant offset and consists of Tx leakage and structural scattering. w is an additive white gaussian noise. Γ is the reflection coefficient. According to (3), y is a function of Γ which is a complex number. Digital modulation schemes, such as ASK, BPSK, and QAM, can be done by manipulating Γ .

Based on (3), the received signals for the MIMO channel, as shown in Fig. 2, can be expressed as follows:

$$\begin{bmatrix} y_1 \\ y_2 \end{bmatrix} = \mathbf{H}^b \begin{bmatrix} \Gamma_1 \\ \Gamma_2 \end{bmatrix} \mathbf{H}^t \begin{bmatrix} x_1 \\ x_2 \end{bmatrix} + \begin{bmatrix} L_1 \\ L_2 \end{bmatrix} + \begin{bmatrix} w_1 \\ w_2 \end{bmatrix} \quad (4)$$

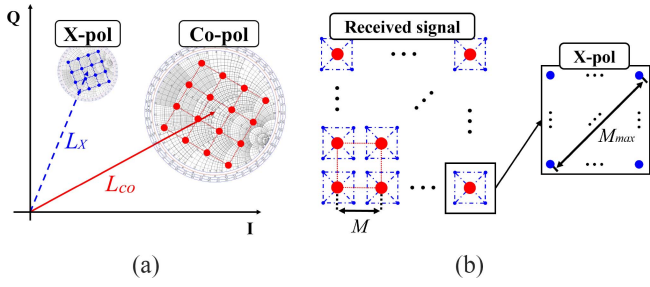


Fig. 3. Received Co-pol and X-pol signals. (a) Received signals on the I/Q plane. (b) Combined received Co- and X-pol signals.

where

$$\mathbf{H}^b = \begin{bmatrix} h_{11}^b & h_{12}^b \\ h_{21}^b & h_{22}^b \end{bmatrix}, \quad \mathbf{H}^t = \begin{bmatrix} h_{11}^t & h_{12}^t \\ h_{21}^t & h_{22}^t \end{bmatrix}.$$

According to (4), Fig. 3 graphically represents how the received signals y_1 and y_2 combine, effectively demonstrating the simultaneous reception of both co-pol and X-pol signals. As the matrix \mathbf{H}^b approaches a diagonal matrix, the signal strength of the X-pol relative to the Co-pol weakens, allowing for the reception of only the intact Co-pol signal. However, when the signal strength of X-pol increases in relation to Co-pol, the components h_{12}^b and h_{21}^b also increase, making it challenging to distinguish between the symbols. In such cases, it is possible to restore the original signal through channel estimation, although this process requires significant computational resources.

To obtain a complete symbol without relying on channel estimation, careful consideration has to be given to the X-pol suppression level, EVM, and modulation factor M . When both the V-pol and H-pol utilize the same square N -QAM modulation scheme, they share the same modulation factor M . To understand the impact of X-pol on the distinction of Co-pol symbols in the superposition of the received signals of y_1 and y_2 , which is the sum of Co-pol and X-pol, is investigated by defining the maximum distance between symbols (M_{\max}) of the X-pol components as $M_{\max} = \sqrt{2}M(\sqrt{N} - 1)$. The values of M and M_{\max} are influenced by the EVM, and as the signal-to-noise ratio (SNR) decreases, the EVM tends to increase. The EVM quantifies the percentage of deviation from the k th reference symbol ($S_{k_{\text{Ref}}}$) to the k th measured symbol ($S_{k_{\text{Mea}}}$). Therefore, the X-pol suppression level, SNR, and modulation coefficient M are important for achieving accurate symbol separation and minimizing the EVM for each received signal y_1 and y_2

$$\text{EVM}(\%) = \tau = \sqrt{\frac{\frac{1}{n} \sum_{k=1}^n |S_{k_{\text{Ref}}} - S_{k_{\text{Mea}}}|^2}{\frac{1}{n} \sum_{k=1}^n |S_{k_{\text{Ref}}}|^2}} \times 100. \quad (5)$$

Consequently, redefining M and M_{\max} becomes necessary when considering EVM. The modulation factor M is defined as $\bar{M} = M(1 - \tau)$, while the maximum distance between symbols M_{\max} is redefined as $\bar{M}_{\max} = M_{\max}(1 + \tau)$.

The received power of the X-pol component is determined by the Co-pol gain G_{co} and the X-pol gain G_X of the antennas in the orthogonal polarization state, as depicted in Fig. 4(a). The power received from the Co-pol component

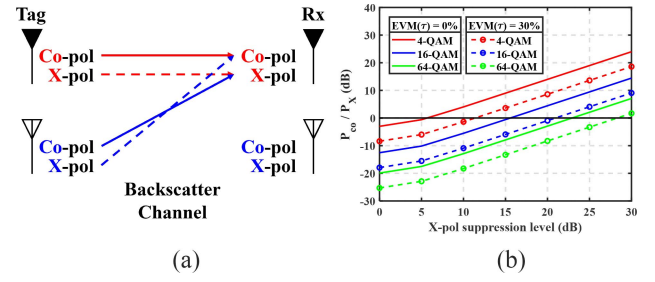


Fig. 4. (a) Co-pol and X-pol signals received at V-pol antenna. (b) Power ratio of P_{co} to P_X over X-pol suppression level.

for a modulation scheme with the shortest distance between symbols (\bar{M}) in the $2 \times 2 \times 2$ MIMO BackCom system can be represented as P_{co} . Similarly, the power received from the X-pol component for a modulation scheme with the longest distance between symbols (\bar{M}_{\max}) can be represented as P_X

$$P_{co} = \frac{P_T G^2 \lambda^4 \bar{M} (G_{co}^2 + G_X^2)}{(4\pi)^4 r^4} \quad (6)$$

$$P_X = \frac{P_T G^2 \lambda^4 \bar{M}_{\max} (G_{co} G_X + G_X G_{co})}{(4\pi)^4 r^4}. \quad (7)$$

Equations (6) and (7) define the X-pol suppression level as the difference between G_{co} and G_X . To ensure the distinction of Co-pol symbols in the presence of X-pol, the condition $P_{co} > P_X$ needs to be satisfied. Fig. 4(b) shows the power ratio of P_{co} and P_X for achievable X-pol suppression levels ranging from 0 to 30 dB, considering EVM values of 0% and 30%. These results indicate that the required level of X-pol suppression varies for the EVM value determined by SNR. Moreover, the choice of an appropriate QAM modulation order can be determined by estimating the theoretical limit where P_{co} is greater than P_X . Estimating EVM in BackCom channels, especially when defining it based on SNR levels, presents unique challenges compared to conventional white Gaussian noise (AWGN) or Rician channels. The complexity arises from the double fading effects inherent in backscatter channels due to the signal's round-trip path. In this study, an SNR of approximately 10 dB is assumed in a typical indoor environment.

To accurately assess a BackCom system's performance, incorporating fading channel models is crucial. While determining the X-pol suppression level related to G_{co} and G_X for dual-channel implementation based on polarization diversity is complex without channel estimation, necessary parameters like symbol separation (M , M_{\max}) and EVM can be effectively determined in an AWGN channel. For instance, Rician channel modeling for multiantenna backscatter tags in indoor environments considers multipath fading, as detailed in [30]. The simulation study showed that the proposed 4-QAM scheme was effective in typical indoor settings with a K-factor of 10 dB, demonstrating its ability to accurately reconstruct the 4-QAM constellation diagram under such conditions. In exceptional cases where the LOS signal strength is significantly low (K-factor below 0.3 dB), 4-QAM symbols may overlap, contrasting with general Rician channels where such overlap does not occur, allowing for accurate determination of M

and M_{\max} values. While Rician fading and AWGN channels show significant differences in communication performance, the method presented in this article for determining the X-pol suppression level remains reliable if symbol separation and EVM can be accurately measured. This consistency enables the design of antennas and RF front-end systems based on an assumed EVM of 30% and an SNR of approximately 10 dB within a typical AWGN scenario. This article presents a proof-of-concept for polarization diversity in dual-channel MIMO BackCom, highlighting its potential for complex fading environments. The proposed method is empirically confirmed through OTA measurements using advanced dual-polarized antennas with metasurface and transceivers, demonstrating the proposed methodology's practicality and suitability for real-world applications.

The OTA measurement setup shown in this article effectively mitigates multipath and fast-fading effects by incorporating EM absorbers around the measurement area. These absorbers help in reducing signal reflections and scattering, thus providing a more controlled environment for accurate OTA measurements. This approach aids in focusing on accurate I/Q modulator modeling based on transfer learning and polarization diversity in BackCom. It also makes the AWGN channel applicable for each Tx and Rx path, simplifying the channel conditions and allowing for a more straightforward analysis of the system's performance.

III. LOAD MODULATOR DESIGN AND MODELING

In this work, a typical analog load modulator design for BackCom was adopted and the fabricated modulator is shown in Fig. 5 [13]. The modulator was fabricated on a low-loss Taconic RF-35 substrate with a thickness of 0.75 mm and a relative dielectric constant (ϵ_r) of 3.5, and a loss tangent ($\tan \delta$) of 0.0018 [31]. The modulator design consists of two enhancement-mode high-electron mobility transistors (E-pHEMTs, Mini-Circuits SAV-541+) in each branch line. The phase difference between branch lines to each the transistor is set to 45 degrees, resulting in a 90-degree phase difference for the backscattered signals, which are then combined using a Wilkinson power divider (WPD). The matching stub of the modulator was optimized to achieve the largest modulation factor within the C-band, utilizing gate bias voltages V_I and V_Q ranging from 0 to 0.6 V. The optimization process involved co-simulation using Keysight ADS, where the S-parameters of the modulator were extracted using a commercial full-wave 3-D finite element method (FEM) simulator, specifically Ansys HFSS 2022 R1.

A. Precise Load Modulator Modeling Using Transfer Learning

In BackCom systems, optimizing the data modulation scheme is crucial for improving performance, similar to other wireless communication systems. However, accurately modeling the nonlinear load modulator in BackCom is challenging due to the discrepancy between the simulation-based optimized reflection coefficients and the actual measured reflection coefficients. Additionally, environmental factors, such as temperature, humidity, and calibration errors, can

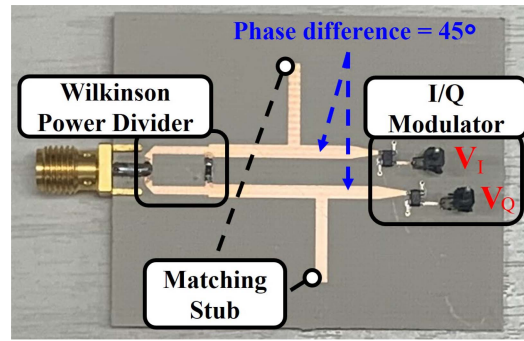


Fig. 5. Fabricated I/Q load modulator for BackCom.

further impact the measured reflection coefficients. To address the challenges associated with load modulator modeling, a transfer learning-based approach is adopted [32]. This technique leverages transfer learning to enhance the accuracy and effectiveness of the load modulator model. By utilizing pre-existing knowledge and models from related tasks, the transfer learning-based approach can overcome the limitations of traditional modeling methods and improve the performance of the load modulator model in BackCom systems. The technique involves the following steps.

1) *Pretraining*: An artificial neural network (ANN) is pre-trained using 3721 simulation data points. The simulation data is obtained by varying the bias voltages V_I and V_Q in the range of 0 to 0.6 V with intervals of 0.01 V. The pretrained ANN consists of three layers with 8, 7, and 6 neurons.

2) *Main Training*: Bias voltages V_I and V_Q are applied using a function generator with 0.1-V increments. The modulator's reflection coefficient is measured using a vector network analyzer (VNA), resulting in 49 measurement data points. These measurement data points are then used to train a fully connected layer with three layers comprising 5, 4, and 3 neurons.

The schematic of the proposed transfer learning technique is shown in Fig. 6, and the measurement environment is illustrated in Fig. 7. The proposed transfer learning model utilizes heuristic techniques to select the best performing model. The generated model produces both the real and imaginary components of the reflection coefficient based on the input V_I and V_Q voltages for modulation in 0.01-V steps. The deviation between the reflection coefficients obtained from the measurement and those derived from the designed model was only 0.81%. The predicted reflection coefficients for all 3721 data points are presented in Fig. 8(b). Utilizing the proposed transfer learning model allows for the rapid generation of numerous predicted reflection coefficients. These predictions provide more precise intervals for both V_I and V_Q , enhancing the model's efficiency and accuracy in its estimations. Moreover, the proposed transfer-learning aligns with the standard complexity of ANNs, and the time and space complexity are negligible for the model owing to the shallow neural network structure [33]. It took approximately 14.2 s to construct the proposed ANN model.

B. Optimal QAM Modulation Scheme

In this section, a method for selecting the optimal QAM modulation constellation based on accurately modeled

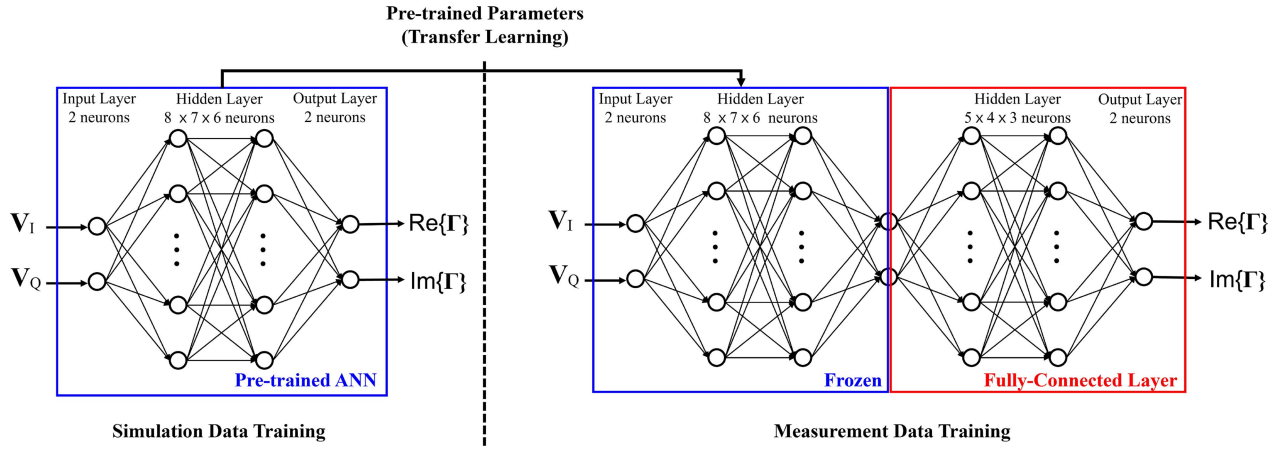


Fig. 6. Proposed transfer learning process for I/Q load modulator modeling.

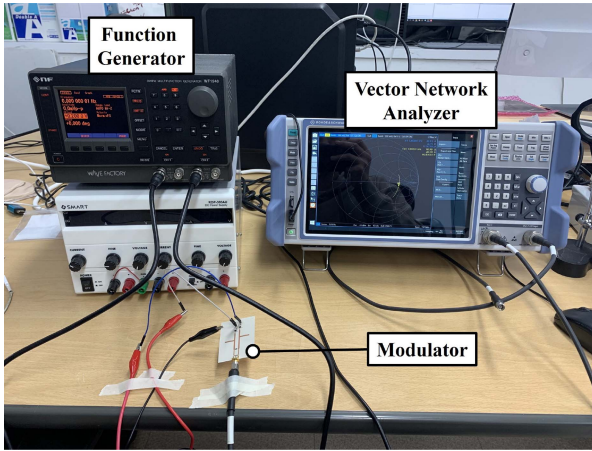


Fig. 7. Measurement setup for a I/Q load modulator.

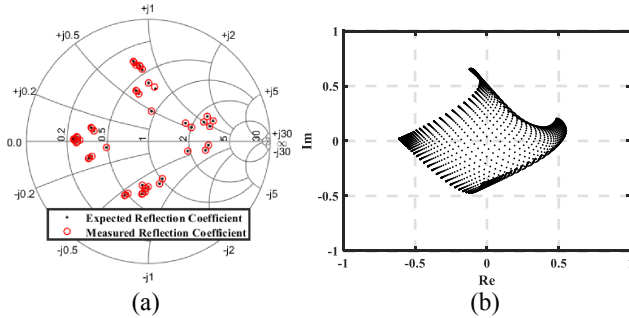


Fig. 8. (a) Expected (simulated) and measured reflection coefficients. (b) Modeled reflection coefficients in I/Q plane.

reflection coefficients in an actual OTA measurement environment is presented. The raw data set of 3721 reflection coefficients at the center frequency of 5.8 GHz, denoted as Γ , undergoes a data alignment process. This alignment step ensures that the reflection coefficients are properly organized and matched to their corresponding QAM modulation constellation points. The aligned data set is then used for further analysis and evaluation of the BackCom system

$$\Gamma = \begin{bmatrix} \text{Re}\{\Gamma\}_i \\ \text{Im}\{\Gamma\}_i \end{bmatrix}, i = 1, \dots, 3721. \quad (8)$$

The indices a , b , c , and d are determined based on the highest and lowest values found in both the real and imaginary

components of Γ , as detailed in

$$\begin{aligned} a &= \arg \max_i \text{Re}\{\Gamma\}_i, & b &= \arg \max_i \text{Im}\{\Gamma\}_i \\ c &= \arg \min_i \text{Re}\{\Gamma\}_i, & d &= \arg \min_i \text{Im}\{\Gamma\}_i. \end{aligned} \quad (9)$$

The corner points are defined as follows:

$$\begin{aligned} \mathbf{k}_a &= \begin{bmatrix} \text{Re}\{\Gamma\}_a \\ \text{Im}\{\Gamma\}_a \end{bmatrix}, & \mathbf{k}_b &= \begin{bmatrix} \text{Re}\{\Gamma\}_b \\ \text{Im}\{\Gamma\}_b \end{bmatrix} \\ \mathbf{k}_c &= \begin{bmatrix} \text{Re}\{\Gamma\}_c \\ \text{Im}\{\Gamma\}_c \end{bmatrix}, & \mathbf{k}_d &= \begin{bmatrix} \text{Re}\{\Gamma\}_d \\ \text{Im}\{\Gamma\}_d \end{bmatrix}. \end{aligned} \quad (10)$$

The four \mathbf{k} vectors correspond to the maximum and minimum values of the real and imaginary parts of Γ for V_I and V_Q . To represent these vectors, a 2×4 \mathbf{K} is used, where the first row contains real numbers and the second row contains imaginary numbers, as shown in

$$\mathbf{K} = [\mathbf{k}_a \ \mathbf{k}_b \ \mathbf{k}_c \ \mathbf{k}_d]. \quad (11)$$

The average value of matrix \mathbf{K} is computed, and this average value is used to remove the offset from the data set Γ

$$\check{\Gamma}_i^T = \Gamma_i^T - \mathbb{E}[\mathbf{K}_i^T], i = 1, 2 \quad (12)$$

where i indicate i th row. By subtracting the average value from each element of Γ , the resulting data set is centered around zero, eliminating any offset that may be present in the original data. This step helps to ensure accurate analysis and processing of the aligned reflection coefficients in subsequent stages of the BackCom system evaluation.

The rotation transformation of \mathbf{K} with respect to θ is expressed as (13), and $\hat{\theta}$ is found by solving the optimization problem in (14a)

$$\bar{\mathbf{k}}_i = \begin{bmatrix} \cos \theta & -\sin \theta \\ \sin \theta & \cos \theta \end{bmatrix} \mathbf{k}_i, i = a, b, c, d \quad (13)$$

$$(P1) : \min_{\theta} \|\mathbf{V}\bar{\mathbf{k}}_a - \mathbf{V}\bar{\mathbf{k}}_d\|^2 + \|\mathbf{V}\bar{\mathbf{k}}_b - \mathbf{V}\bar{\mathbf{k}}_c\|^2 \quad (14a)$$

$$\text{s.t.} \|\mathbf{V}\bar{\mathbf{k}}_a - \mathbf{V}\bar{\mathbf{k}}_d\| = \|\mathbf{V}\bar{\mathbf{k}}_b - \mathbf{V}\bar{\mathbf{k}}_c\| \quad (14b)$$

where

$$\mathbf{V} = \begin{bmatrix} 1 & 0 \\ 0 & 0 \end{bmatrix}.$$

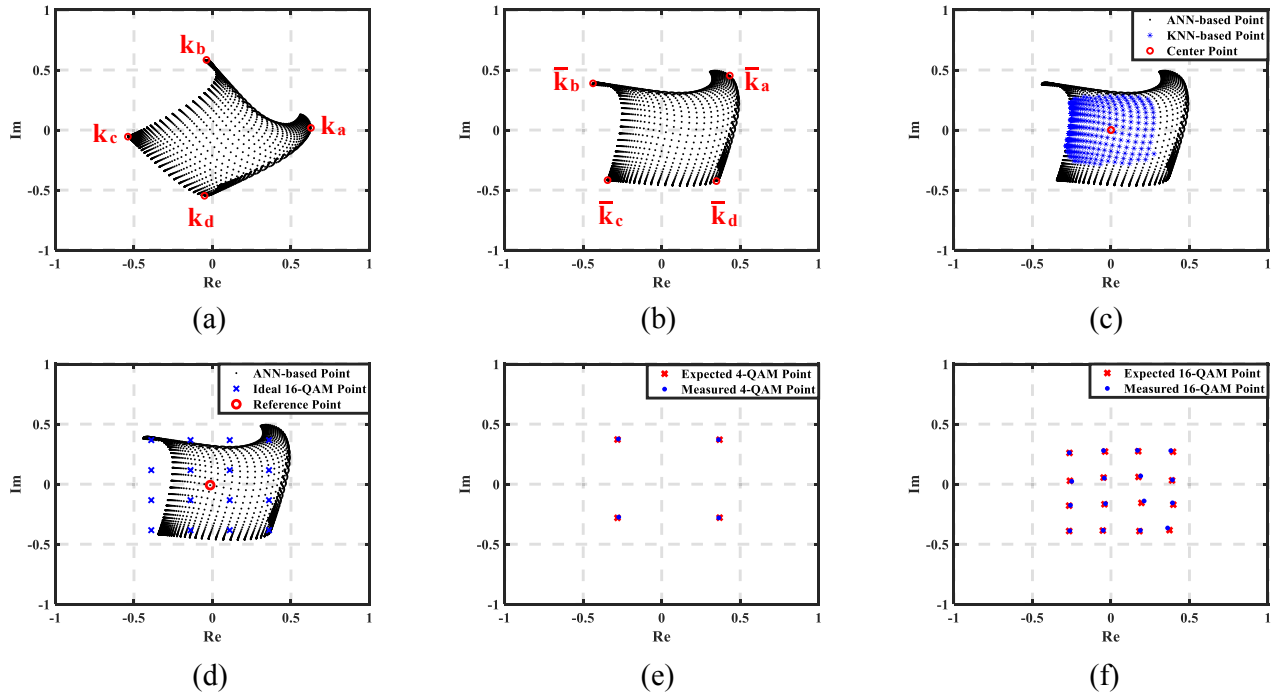


Fig. 9. Systematic approach for finding an optimized QAM constellation. (a) Reflection coefficient values. (b) Rearranged (rotated) reflection coefficients. (c) Reference point identification through k-NN algorithm. (d) Square 16-QAM constellation points on reflection coefficient values. (e) Expected (simulated) and measured optimized 4-QAM constellation. (f) Expected and measured optimized 16-QAM constellation.

Once the optimal $\hat{\theta}$ is found, $\check{\Gamma}$ can be correctly arranged by performing the rotation transformation. The resulting alignment is shown in Fig. 9(b)

$$\bar{\Gamma} = \begin{bmatrix} \cos \hat{\theta} & -\sin \hat{\theta} \\ \sin \hat{\theta} & \cos \hat{\theta} \end{bmatrix} \check{\Gamma}. \quad (15)$$

To perform QAM modulation by selecting N points from a properly arranged $\bar{\Gamma}$, the choice of which points to select can significantly impact the modulation factor and overall performance. In this study, an square N -QAM is established as the evaluation benchmark and compared with $\bar{\Gamma}$ to determine the optimal QAM constellation performance.

The square N -QAM constellation is generated using the k -nearest neighbor (k-NN) algorithm based on the average vector of $\bar{\mathbf{k}}$ (computed from \mathbf{k}_a , \mathbf{k}_b , \mathbf{k}_c , and \mathbf{k}_d). Using the Euclidean distance metric, 600 center points denoted as $\check{\Gamma}_\ell$ are established, where $\ell = 1, \dots, 600$. These 600 center points are deemed sufficient for achieving optimal QAM performance.

The square N -QAM constellation points denoted as \mathbf{q}_i are modeled by adding the amplitudes $A_c, A_s \in \{\pm(\mathbf{d}/2), \pm(3\mathbf{d}/2), \dots, \pm[(\sqrt{N}-1)\mathbf{d}/2]\}$ composed of arbitrary real number \mathbf{d} , to the 600 center points of $\check{\Gamma}_\ell$, and the constellation set \mathbf{Q} is expressed as (15)

$$\begin{aligned} \mathbf{Q} &= \{\mathbf{q}_i | \forall \mathbf{d} \in \mathbb{R}\}, \\ \mathbf{q}_i &\triangleq A_c \hat{\mathbf{a}}_{\text{re}} + A_s \hat{\mathbf{a}}_{\text{im}} + \check{\Gamma}_\ell, \quad i = 1, \dots, N \end{aligned} \quad (16)$$

where $\hat{\mathbf{a}}_{\text{re}}$ and $\hat{\mathbf{a}}_{\text{im}}$ are unit vectors for the real and imaginary parts, respectively.

The modeled square N -QAM consists of N symbols, and the matrix $\hat{\Gamma}_i$ is formed by selecting reflection coefficients that

exist at the shortest Euclidean distance for \mathbf{q}_i , one by one

$$\hat{\Gamma}_i = \arg \min_{\bar{\Gamma}} \sqrt{(\bar{\Gamma} - \mathbf{q}_i)^2}, \quad i = 1, \dots, N. \quad (17)$$

The difference between $\hat{\Gamma}_i$ and the symbols of the square N -QAM is accumulated and defined as ϱ

$$\varrho = \sum_{i=1}^N \sqrt{(\hat{\Gamma}_i - \mathbf{q}_i)^2}. \quad (18)$$

To find an optimized QAM constellation, the minmax algorithm of (19) is performed on the difference ϱ and the distance \mathbf{d} between arbitrary symbols

$$\Gamma_{\text{opt}} = \arg \max_{\mathbf{d}} \min_{\varrho} \hat{\Gamma}. \quad (19)$$

The optimization results for 4-QAM and 16-QAM modulation schemes, achieved through transfer learning for the center frequency band of interest, are presented in Fig. 9(e) and (f), respectively. These optimizations resulted in EVM values of 1.59% and 3.49%, respectively. Table I provides the corresponding V_I and V_Q values used for generating the optimized QAM constellations. It is important to note that the optimization technique described is not limited to these specific modulation orders and can be extended to higher order modulations as well. The QAM constellations exhibit rotation of the reflection coefficients, which is proportional to the wavelength difference from the center frequency. Fig. 10 illustrates the constellations where the optimization is maintained across the given BW (5.725 ~ 5.875 GHz), showcasing the robustness and effectiveness of the proposed technique.

TABLE I
OPTIMIZED BIAS VOLTAGE FOR 4- AND 16-QAM

| 4-QAM (V_I, V_Q) | 16-QAM (V_I, V_Q) | | | |
|-------------------------|--------------------------|--------------|--------------|--------------|
| (0.11, 0.16) | (0.17, 0.19) | (0.15, 0.24) | (0.17, 0.29) | (0.19, 0.60) |
| (0.09, 0.34) | (0.23, 0.20) | (0.22, 0.25) | (0.23, 0.30) | (0.24, 0.60) |
| (0.31, 0.41) | (0.31, 0.02) | (0.26, 0.24) | (0.27, 0.29) | (0.28, 0.42) |
| (0.41, 0.03) | (0.52, 0.14) | (0.34, 0.23) | (0.35, 0.28) | (0.39, 0.36) |

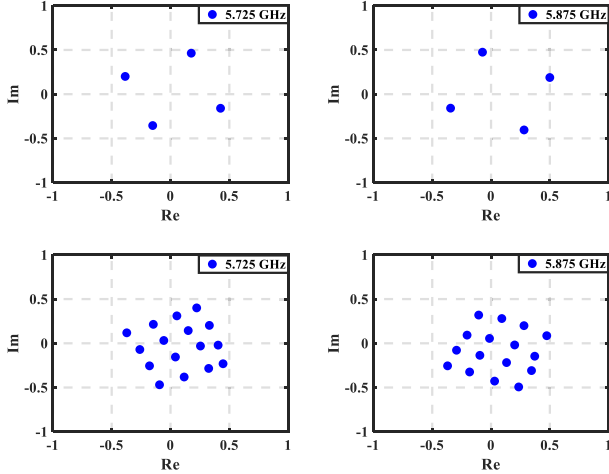


Fig. 10. Measured 4- and 16-QAM constellation diagrams over a bandwidth of 150 MHz.

C. Energy Efficiency Analysis

One of the advantages of optimized QAM modulation is its high-energy efficiency. It is important to consider energy efficiency in wireless communication systems for IoT, as it directly impacts the overall power consumption and battery life of devices. By minimizing the power consumption of the modulator, the energy efficiency of the BackCom system can be enhanced, making it well-suited for low-power and sustainable IoT applications. The majority of the DC power is consumed by E-pHEMTs consisting of the proposed analog I/Q load modulator. The DC power consumption can be calculated using (19). By dividing P_{DC} by the data rate, the energy per bit can be determined. Furthermore, optimizing the QAM modulation scheme enables higher data rates while maintaining the energy per bit (energy efficiency)

$$P_{DC} = \frac{1}{2} CV^2 f_s \quad (20)$$

where C represents the gate capacitance, f_s represents the switching speed, and V represents the applied gate voltage.

Based on the provided information, the DC power consumption of the designed modulator can be calculated for both 4-QAM and 16-QAM modulations.

For 4-QAM modulation, the first FET has a power consumption of $3.4 \mu\text{W}$, and the second FET consumes $3.6 \mu\text{W}$, resulting in a total energy consumption of $7 \mu\text{W}$. Similarly, for 16-QAM modulation, the first FET consumes $4.7 \mu\text{W}$, and the second FET consumes $5.5 \mu\text{W}$, resulting in a total energy consumption of $10.2 \mu\text{W}$. Comparing these values to the power consumption when using a voltage range of 0 to 0.6 V (taking the average of 0.3 V) without optimization, both 4-QAM and 16-QAM consume a total of $11.7 \mu\text{W}$ of

power. This indicates that the optimized QAM modulation results in lower power consumption, highlighting the energy efficiency achieved through the proposed optimization process. It is important to note that as the data rate increases, the switching speed also increases, which can lead to higher DC power consumption.

Therefore, the optimization process not only improves the EVM performance but also offers energy efficiency benefits, making it advantageous for BackCom systems. It should be noted that this optimization process is particularly beneficial when managing multiple backscatter tags within the same environment. It is highly probable that I/Q load modulators designed through the same manufacturing process in a similar working environment have a similar optimal QAM scheme. A one-time machine learning-based optimization process of a single tag is able to enhance the overall system performance of the BackCom system, particularly in the presence of multiple backscatter tags. The additional power consumption at the backscatter node required for training the transfer learning-based ANN is estimated to be approximately $410.1 \mu\text{W}$, based on 16-QAM as a reference. This additional power consumption arises from selecting an additional 33 bias points compared to the 16 bias points selected for 16-QAM. It should be noted that the implementation of the proposed backscattering system eliminates the need for conventional wireless systems, such as WiFi, ZigBee, or Bluetooth for node communication. Moreover, the proposed system consumes less than 0.6 mW, which is significantly lower than the tens of mW typically required by conventional wireless systems for transmitting signals.

IV. RF FRONT-END SYSTEM FOR MIMO BACKCOM

Fig. 11 shows the block diagram of the proposed MIMO transceiver system designed for BackCom applications, employing a 2×2 MIMO transceiver structure [34], [35]. The system incorporates a voltage controlled oscillator (VCO) that generates an output frequency of 5.8 GHz with a power of 2 dBm. This signal is then amplified by two power amplifiers, PA1 and PA2, which provide gains of 11.5 and 10 dB, respectively. The amplified signal is divided into two equal power signals using a WPD, which achieves a power split of 3 dB. Each of these signals is then transmitted via two transmit (Tx) antennas, enabling the radiation of a 5.8-GHz continuous wave (CW) signal.

For the Rx chain of the system, the backscattered signal received by the Rx antenna is first amplified by a low-noise amplifier (LNA) with a gain of 21.6 dB. The amplified signal is then mixed with the signal obtained from the 20-dB coupled line coupler. This mixing process takes place in the mixer and results in the generation of a baseband signal through direct down-conversion. In the proposed BackCom system, even a small difference in the tone of the received signals can have a significant impact when directly down-converted. To address this issue, the CW signal with the same tone is distributed and used as the input to the WPD. Each baseband signal is then processed separately. A total of four signals are collected

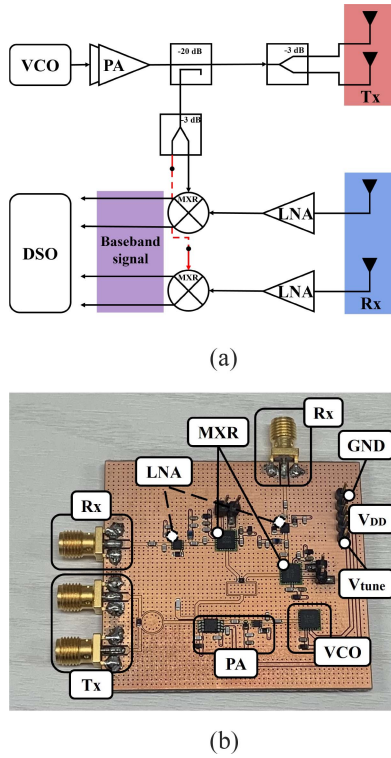


Fig. 11. Proposed 2×2 MIMO transceiver system for BackCom: (a) system block diagram and (b) fabricated system.

using a digital storage oscilloscope (DSO) for further analysis and evaluation.

The collected signals obtained from the MIMO transceiver system were processed and analyzed using MATLAB. The transceiver system was implemented on commercially available FR-4 substrate with a thickness of 1 mm and dimensions of $58 \times 52.6 \text{ mm}^2$. The FR-4 substrate used in the printed circuit board (PCB) has a relative dielectric constant (ϵ_r) of 4.14 and a loss tangent ($\tan \delta$) of 0.02. The proposed MIMO transceiver system for BackCom shown in Fig. 11 was employed for the measurements. The measured output power levels of Tx1 and Tx2 ports were 14.5 dBm. Table II shows a detailed list of components used in the designed MIMO transceiver system.

V. ANTENNA DESIGN

As shown in Fig. 4(b), the antenna plays a crucial role in implementing polarization diversity by providing high-X-pol suppression levels and SNR improvements. Increasing the antenna gain is a straightforward approach to enhance SNR, especially when dealing with limited transmitter power. In this article, a dual-polarized Vivaldi antenna is employed to achieve high gain and suitable X-pol suppression levels. Vivaldi antennas are renowned for their wide BW, low-cross-polarization, and high-gain characteristics, making them an excellent choice for the proposed MIMO BackCom system [36].

The curved line $f_1 = 3.93 \times e^{(30x)} - 3.3 \text{ mm}$, which constitutes the radiator, is expressed in terms of x and spans a range from 0 to 84 mm. Additionally, $f_2 = -5133 \times e^{(0.23x)} +$

TABLE II
COMPONENT LIST

| Component | Model @Manufacturer | Specification |
|-----------|--------------------------------------|---|
| VCO | HMC431LP4ETR @Analog Devices | Freq. range: 5.5-6.1 Ghz Output power: 2 dBm |
| PA1 | GRF2505 @Guerrilla RF | Gain: 11.5 dB NF: 1.2 dB |
| PA2 | HMC407MS8GE @Analog Devices | Gain: 10 dB NF: 5.5 dB |
| LNA | HQPL9503TR7 @Qorvo | Gain: 21.6 dB NF: 0.9 dB |
| MXR | HMC951A @Analog Devices | LO power: 2 dBm Conversion Gain: 13dB |
| DSO | WaveRunner 604Zi @Teledyne LeCroy | Sampling rate: 40 GS/s Resolution: 8-bits |

$0.012 \times e^{(-0.18x)} \text{ mm}$ and $f_3 = (1.28 \times 10^{13}) \times e^{(0.946x)} - 0.133 \times e^{(-0.137x)} \text{ mm}$ are also expressed as exponential functions with respect to x , where the range of x for f_2 is from -42 to -30 mm , and the range of x for f_3 is from -34 to -30 mm . As a result, antennas 1 and 2 have radiators with nearly identical structures and are only slightly deformed by the assembly slots.

To ensure effective excitation and maintain a reflection coefficient below -10 dB within the operational frequency band, a radial stub was incorporated into the design. In the V-pol antenna (antenna 1), a small rectangular metal patch structure was used to establish a galvanic connection with the radiator of the H-pol antenna (antenna 2). The two antennas were separated by a slot specifically designed for dual-polarization assembly, positioned orthogonally to each antenna. Additionally, to further enhance the gain and improve the SNR, corrugations and metasurface structures were incorporated into the antenna design, as illustrated in Fig. 12. These elements contributed to an overall increase in antenna gain and resulted in improved system performance. Detailed antenna design parameters are summarized in Table III. The effects of corrugation and metasurface are discussed in below. The effects of corrugation and metasurface structures in the antenna design are as follows.

1) *Corrugation*: A corrugation structure in the form of a slot array was implemented at the edge of the radiator. This slot array consists of slots with specific dimensions, forming an anisotropic impedance surface. The width of each slot is $\lambda_g/4$, and the height is $\lambda_g/10$, where λ_g represents the guided wavelength. This structure creates a high-impedance surface in the vertical direction (z-direction) relative to the electric field, while maintaining a low-impedance surface in the horizontal direction. The purpose of this design is to suppress side lobes and improve the antenna's gain [37]. The width W_2 and height L_2 of the slot for the designed corrugation structure in this article are shown in Table III.

2) *Metasurface*: A metasurface with double negative (DNG) electromagnetic properties was designed in this work, specifically targeting negative permittivity (ϵ) and negative permeability (μ) within the C-band frequency range. To analyze the proposed metasurface, the ϵ and μ values were extracted based on the S-parameters, utilizing the meta-atom configuration within the experimental setup depicted in Fig. 13(a) [38], [39]. The resulting ϵ and μ values

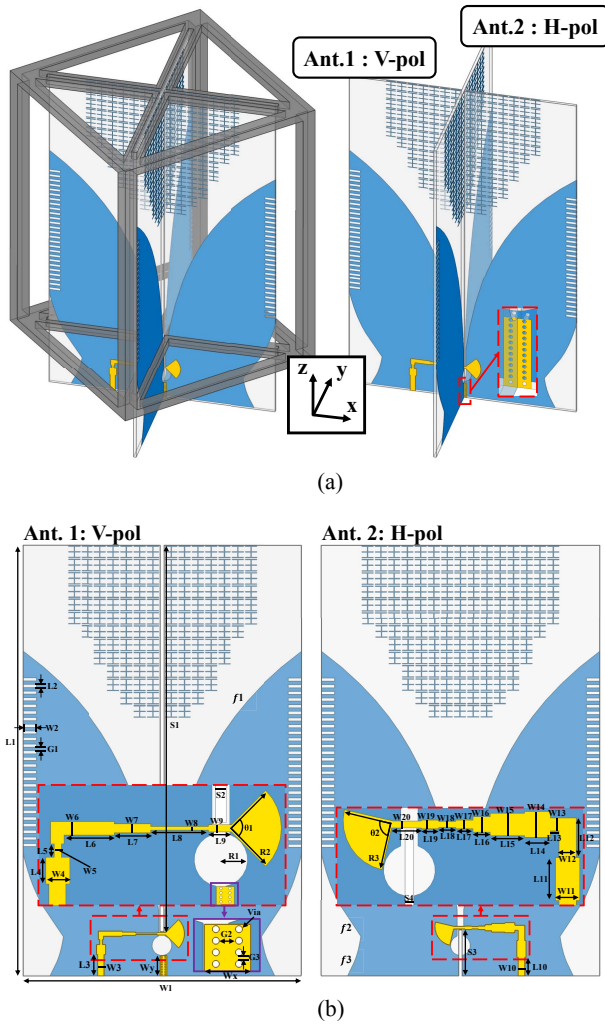


Fig. 12. Antenna geometry. (a) 3-D view of the assembled dual polarized vivaldi antenna. (b) Planar view of the vivaldi antenna.

TABLE III
ANTENNA DESIGN PARAMETERS IN MM

| | | | | | | | |
|------------|------------|----------|-----|----------|------|------------------|------------|
| L_1 | 130 | L_2 | 1 | L_3 | 6.4 | L_4 | 3 |
| L_5 | 1.5 | L_6 | 5.6 | L_7 | 4.1 | L_8 | 6.5 |
| L_9 | 2.6 | L_{10} | 5.6 | L_{11} | 5 | L_{12} | 4.6 |
| L_{13} | 1 | L_{14} | 3 | L_{15} | 4 | L_{16} | 2 |
| L_{17} | 2 | L_{18} | 2 | L_{19} | 2 | L_{20} | 3.5 |
| L_{21} | 3.3 | L_{22} | 3.5 | W_1 | 84 | W_2 | 4 |
| W_3 | 1.9 | W_4 | 2.7 | W_5 | 0.8 | W_6 | 1.5 |
| W_7 | 1 | W_8 | 0.4 | W_9 | 0.8 | W_{10} | 2 |
| W_{11} | 2.8 | W_{12} | 2 | W_{13} | 1.5 | W_{14} | 3 |
| W_{15} | 2.6 | W_{16} | 1.8 | W_{17} | 1 | W_{18} | 0.7 |
| W_{19} | 1 | W_{20} | 0.8 | W_{21} | 0.1 | W_{22} | 0.1 |
| G_1 | 1 | G_2 | 0.7 | G_3 | 0.2 | G_4 | 1.6 |
| S_1 | 116.7 | S_2 | 1.2 | S_3 | 13.8 | S_4 | 1 |
| R_1 | 3 | R_2 | 6 | R_3 | 5.8 | θ_1 | 90° |
| θ_2 | 90° | W_x | 2 | W_y | 6.1 | Via [†] | 0.3 |

*† Cylindrical via diameter

exhibit negative values across the entire frequency band of interest as shown in Fig. 13(c). This DNG structure enables the improvement of antenna gain by leveraging the negative refractive index and phase [40], [41].

Fig. 14 illustrates the enhanced gain achieved for both the V-pol and H-pol antennas through the incorporation of

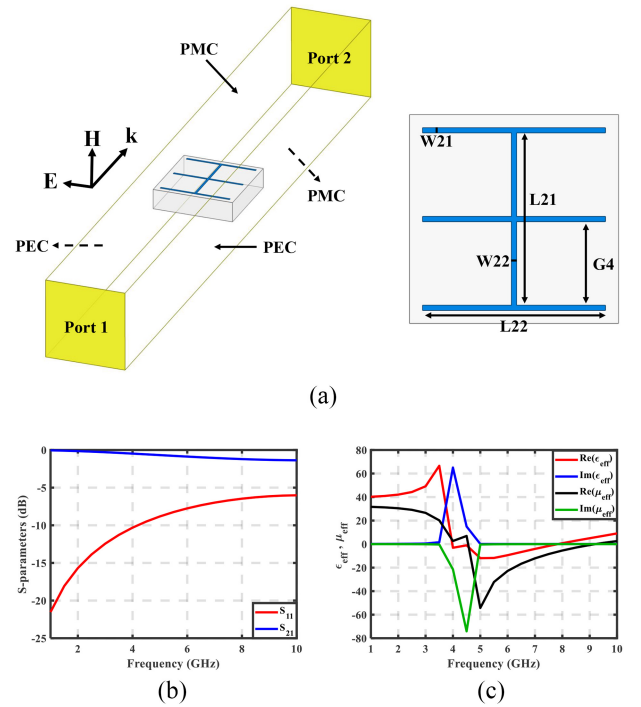


Fig. 13. (a) Meta-atom design for metasurface: Simulation setup and unit cell (meta-atom). (b) Simulated reflection and transmission coefficients. (c) Extracted equivalent complex constitutive parameters (ϵ_{eff} and μ_{eff}).

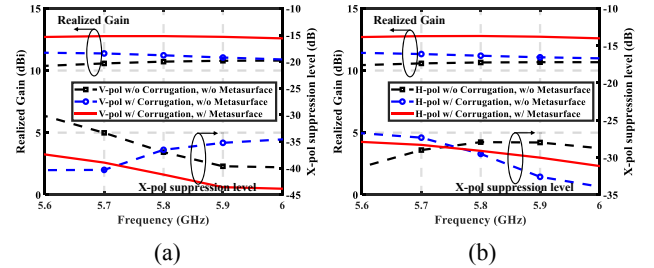


Fig. 14. Antenna gain and X-pol suppression level with and without corrugation and metasurface: (a) V-pol and (b) H-pol.

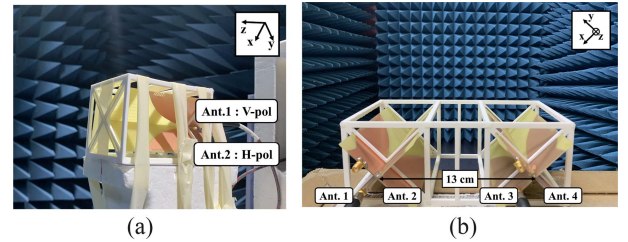


Fig. 15. Antenna measurement setup. (a) Single antenna. (b) Transmit and receive antennas.

corrugation and metasurface structures. It should be noted that the X-pol suppression level remains at a moderate level, demonstrating its suitability for implementation in MIMO BackCom systems.

VI. ANTENNA MEASUREMENT

The high-gain Vivaldi antenna integrated with a metasurface was fabricated using a 1-mm thick FR-4 substrate with relative permittivity (ϵ_r) of 4.14 and loss tangent ($\tan \delta$) of 0.02. A

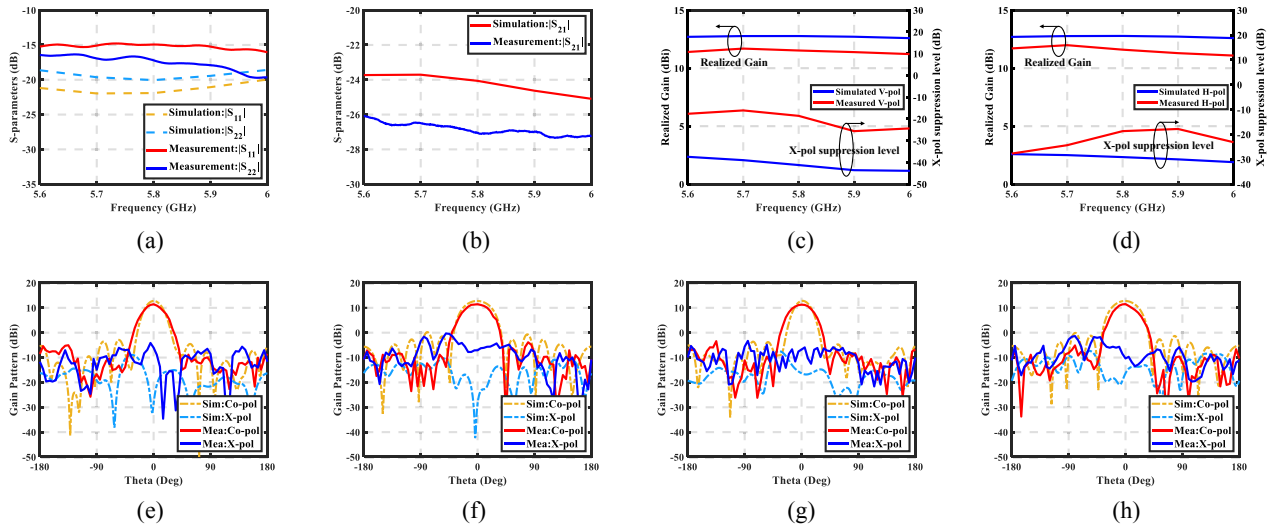


Fig. 16. Measured and simulated antenna performances. (a) Reflection coefficient. (b) Transmission coefficient. (c) V-pol antenna gain values over frequency at boresight. (d) H-pol antenna gain values over frequency at boresight. (e) Antenna gain patterns at $\phi = 0^\circ$ (V-pol). (f) $\phi = 90^\circ$ (V-pol). (g) $\phi = 0^\circ$ (H-pol). (h) $\phi = 90^\circ$ (H-pol).

3D-printed fixture was employed, to hold two Vivaldi antennas together tightly. The incremental effects of the 3D-printed frame on the antenna's performance were observed, revealing a similarity between the combined antenna and the simulation results. The printed fixture played a crucial role in maintaining the antenna position, minimizing polarization mismatch, and preserving antenna performance.

The fabricated antenna was measured in an anechoic chamber for performance evaluation as shown in Fig. 15(a). Both the V-pol and H-pol of the fabricated antenna satisfied the requirement of having reflection coefficients below -10 dB in the C-band. The measured transmission coefficient between the ports (cross-pol coupling) was found to be less than -26 dB as shown in Fig. 16(b). The radiation patterns at the center frequency is also shown in Fig. 16(e)–(h). Fig. 16(c) and (d) represents the gain versus frequency for $\theta = 0$ and $\phi = 0$. While the X-pol suppression experiences slight reduction due to manufacturing errors, a theoretical X-pol suppression level of 12 dB or higher at an EVM of 30% is sufficient for implementing the polarization diversity of 4-QAM, as depicted in Fig. 4(b).

The measured X-pol suppression levels ranging from 15 to 20 dB are sufficient for implementing polarization diversity in the BackCom system for 4-QAM modulation, as discussed in Section II-B. Both the V-pol and H-pol exhibit high-realized gain values exceeding 11.5 dBi within the operating frequency band, and the SNR was measured at 11 dB. Based on the parametric study presented in Fig. 17(a), the optimal isolation was achieved when the distance between the Tx and Rx antennas was 13 cm. This high-isolation level is attributed to the structural effect of the antenna being slanted at a 45-degree angle. To securely position the Tx and Rx antennas, a 3D-printed frame was designed, as shown in Fig. 15(b). The measured isolation between the Tx and Rx antennas is shown in Fig. 17(b). The proposed antenna configuration for the RF front-end system demonstrates a significant level of isolation, with values below -40 dB for both Tx and Rx. This substantial

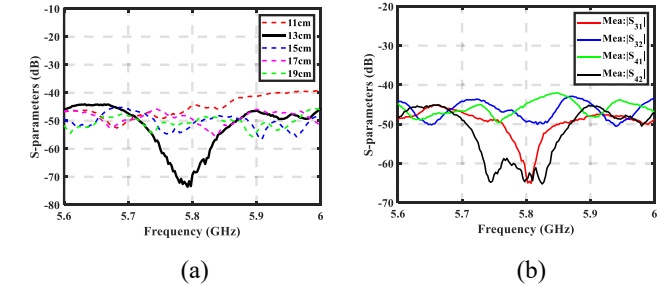


Fig. 17. (a) Isolation between antenna2 and antenna4 according to distance. (b) Coupling between Tx and Rx antennas.

isolation contributes to reducing Tx leakage to the Rx chain and renders the designed RF front-end system well-suited for BackCom applications.

VII. BACKSCATTER COMMUNICATION MEASUREMENT

Fig. 18 shows the proposed measurement environment for the MIMO BackCom system, which includes the MIMO transceiver, antennas, and modulator tags. The spacing between the tag and the transceiver was set at $11.6 \lambda_0$, where λ_0 is the wavelength in free space. The V-pol and H-pol modulators were modulated using bias voltages V_I and V_Q , respectively. These modulators implemented the optimized QAM scheme derived from transfer learning-based modulator modeling, as shown in Table I. The modulators of the backscattering tags were driven by a function generator. Due to the limitations of the equipment's BW, the generated pulse had a BW of 4 MHz. To validate the proposed $2 \times 2 \times 2$ MIMO BackCom system, three frequency points were selected at low, center, and high-frequency ranges. The received backscattered data was captured using a DSO, and the collected data was subsequently processed using MATLAB for further analysis and evaluation. Due to the presence of I/Q imbalance in the collected raw data, a compensation process

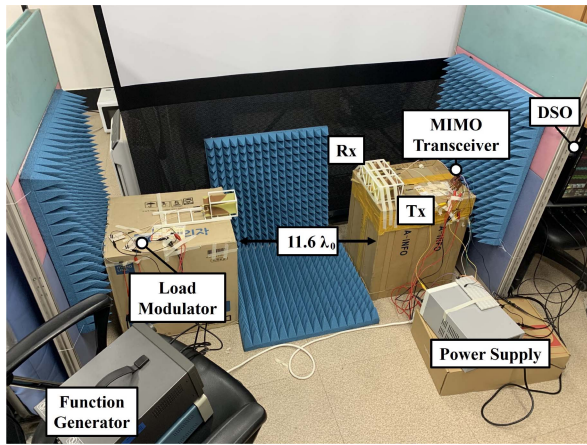


Fig. 18. OTA measurement setup.

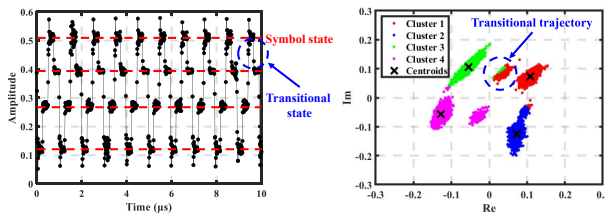


Fig. 19. Received BackCom signal at transitional state.

was applied to mitigate the imbalance issue. A constellation diagram of the H-pol data at the center frequency after I/Q compensation is shown in Fig. 19, and the pulse signal generated by the function generator exhibited a transient state, resulting in a transitional trajectory. To eliminate this transitional trajectory, the k -means clustering algorithm was employed. Assuming backscattering of the 4-QAM signal, four symbol sections (*Symbol 1*, *Symbol 2*, *Symbol 3*, and *Symbol 4*) were expected. s

As a result, the pulse formed four clusters representing the four symbol states, with transitional trajectories occurring during transitions between symbols. This transitional trajectory, considered as packet loss that fails to discriminate symbols, resulted in the removal of approximately 20% of the data farthest from each centroid. Therefore, Fig. 20 presents the properties of the OTA measurements for 4-QAM and 16-QAM of H-pol as a single channel after signal processing at low, central, and high frequencies, with an average EVM of 5.9% in 4-QAM and 6.3% in 16-QAM. The presented constellation diagram shows the effectiveness and practicality of the proposed QAM optimization regarding frequency BW in an OTA environment. The design of the proposed antenna features robust broadband impedance matching between the antenna and the modulator. This highlights the significance of load modulator modeling over the antenna's position or allocation. The diagram displays uniform constellation patterns at a distance of $11.6 \lambda_0$, consistently observed across the operational frequency BW, under the condition that the far-field requirements are met.

For the measured EVM value of approximately 6%, the I/Q modulators performing the same QAM modulation should

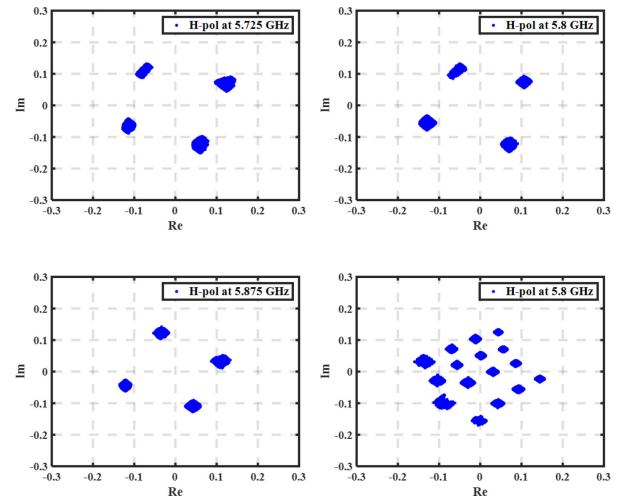


Fig. 20. Measured 4- and 16-QAM single channel constellation diagrams.

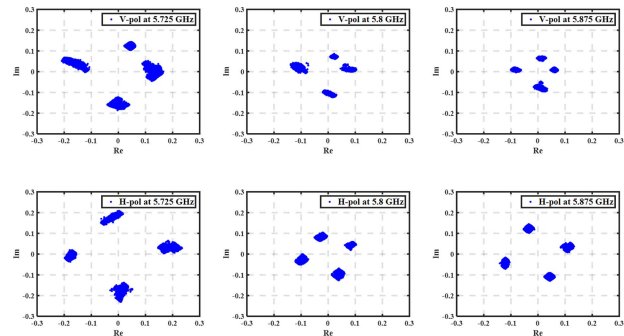


Fig. 21. Measured 4-QAM dual channel constellation diagrams.

have an X-pol suppression level of at least 6.8 dB in 4-QAM and 16.7 dB in 16-QAM, as calculated based on (6) and (7). The Vivaldi antenna used in the study exhibits a X-pol suppression level of around 18 dB, which is sufficient for implementing dual channels of both 4-QAM and 16-QAM. Fig. 21 shows six constellation diagrams of 4-QAM measured in OTA for dual channels, where V-pol and H-pol each exhibited an average 9.35% EVM performance. It is worth noting that V-pol had a lower modulation factor than H-pol. The discrepancy noted in this article primarily stems from manufacturing errors, such as issues with soldering, fabrication, or packaging of modulators. While commercial transistors and PCB processes exhibit minor errors, making a single modulator model generally sufficient. The discrepancies observed in OTA measurements are primarily attributed to the manual assembly and soldering processes of circuits. Automated manufacturing process can reduce such discrepancies. However, when discrepancies arise, as noted in this study, it's essential to separately compute the modulation coefficients for V-pol and H-pol, adjusting them according to the specified equations shown in (6) and (7). In the 150-MHz BW, \bar{M} was found to be the smallest compared to \bar{M}_{\max} when calculating the P_{CO} of V-pol and P_X of H-pol at 5.875 GHz. In this case, \bar{M}_{\max} was found to be 3.28 times larger than \bar{M} . Based on these results, the required X-pol suppression level is calculated to be 17.5 dB or more for 4-QAM and 27 dB or more for

TABLE IV
PERFORMANCE COMPARISON TABLE

| Reference | Frequency | N -QAM | EIRP | MIMO | Modulation Type | Data Rate | Spectral Efficiency | Energy Efficiency | EVM | Range (OTA) |
|-----------------|-----------|----------|--------|------|-----------------|-----------|---------------------|-------------------|---------|------------------|
| [8] | 915 MHz | 16-QAM | 36 dBm | × | Digital | 96 Mbps | 1.2 bps/Hz | 15.5 pJ/bit | 9.38 % | 3.8 λ_0 |
| [9] | 5.8 GHz | 32-QAM | 36 dBm | × | Digital | 2.5 Mbps | 3.3 bps/Hz | 45.2 pJ/bit | 4.60 % | 19.3 λ_0 |
| [11] | 24.5 GHz | 16-QAM | 47 dBm | × | Analog | 2.0 Gbps | 0.5 bps/Hz | 0.17 pJ/bit | 12.37 % | 40.8 λ_0 |
| [12] | 2.45 GHz | 16-QAM | N/A | × | Analog | 960 Mbps | 2.0 bps/Hz | 0.061 pJ/bit | 8.37 % | Wired |
| [13] | 2.45 GHz | 16-QAM | N/A | × | Analog | 120 Mbps | 2.0 bps/Hz | 6.7 pJ/bit | 16.76 % | Wired |
| Proposed | 5.8 GHz | 4-QAM | 26 dBm | ○ | Analog | 300 Mbps | 2.0 bps/Hz | 0.047 pJ/bit | 9.35 % | 11.6 λ_0 |

* λ_0 is the free-space wavelength at the center operating frequency.

16-QAM. Consequently, the X-pol suppression level of the antenna used is approximately 18 dB, making it theoretically challenging to implement 16-QAM MIMO BackCom, which aligns with the measurement results. It is also important to note that the \bar{M}_{\max} used in the calculation of (7) sets the theoretical upper bound by considering the power of P_X based on the maximum modulation factor observed diagonally between symbols. If P_X varies according to changes in the distance between the tag and receiver and multipath conditions, there is a possibility for MIMO BackCom to operate even when the X-pol suppression level calculated from (7) is at the level calculated as $\bar{M}_{\max}/\sqrt{2}$.

On the other hand, the I/Q load modulator mismatch problem can be effectively reduced by using an automated fabrication process. However, it is crucial to emphasize that the required X-pol suppression level varies significantly with the degree of inconsistency, as shown in the previous results. Therefore, this result highlights the feasibility and effectiveness of utilizing the proposed transfer learning-based approach for modeling and implementing higher order modulation schemes in MIMO BackCom systems.

The power consumption, calculated using (19), was found to be 0.047 pJ/bit for both 4-QAM MIMO BackCom, considering the energy per bit with a BW of 150 MHz. With 4-QAM, the data rate is doubled through the dual polarization channel, enabling data rates of 300 Mb/s within a 150-MHz BW in the C-band.

Table IV provides a comparison of the proposed MIMO BackCom system with those from other studies focusing on high-order modulation. By implementing polarization diversity and utilizing dual channels, the proposed BackCom system achieved improved data rates within the allowed BW of the ISM band. Furthermore, despite being a dual-channel system, the proposed transfer learning-based modeling demonstrated superior EVM performance while maintaining energy efficiency.

VIII. CONCLUSION

This article introduces a novel approach for enhancing dual-polarized MIMO BackCom systems utilizing transfer learning-based modulation optimization. The study focuses on accurately modeling the I/Q load modulator for optimized higher order modulation schemes using transfer learning techniques, which exhibits robust performance in real OTA measurement environments. Moreover, the proposed optimized modulation scheme maintains consistency across a wide

operating frequency BW of 150 MHz and offers high-energy efficiency. This article also includes the first OTA measurements of a dual-polarization BackCom system, providing valuable insights into the implementation requirements for MIMO BackCom. The use of dual channels and dual polarization demonstrates significant enhancements in data rates, particularly with higher order modulation. These research findings are expected to have a substantial impact on the progress of IoT technology.

REFERENCES

- [1] E. Sisinni, A. Saifullah, S. Han, U. Jennehag, and M. Gidlund, "Industrial Internet of Things: Challenges, opportunities, and directions," *IEEE Trans. Ind. Informat.*, vol. 14, no. 11, pp. 4724–4734, Nov. 2018.
- [2] Y. A. Qadri, A. Nauman, Y. B. Zikria, A. V. Vasilakos, and S. W. Kim, "The future of healthcare Internet of Things: A survey of emerging technologies," *IEEE Commun. Surveys Tuts.*, vol. 22, no. 2, pp. 1121–1167, 2nd Quart., 2020.
- [3] S. N. Daskalakis, J. Kimionis, A. Collado, G. Goussetis, M. M. Tentzeris, and A. Georgiadis, "Ambient backscatterers using FM broadcasting for low cost and low power wireless applications," *IEEE Trans. Microw. Theory Techn.*, vol. 65, no. 12, pp. 5251–5262, Dec. 2017.
- [4] O. Elijah, T. A. Rahman, I. Orikumbi, C. Y. Leow, and M. N. Hindia, "An overview of Internet of Things (IoT) and data analytics in agriculture: Benefits and challenges," *IEEE Internet Things J.*, vol. 5, no. 5, pp. 3758–3773, Oct. 2018.
- [5] F. Zhu, Y. Lv, Y. Chen, X. Wang, G. Xiong, and F.-Y. Wang, "Parallel transportation systems: Toward IoT-enabled smart urban traffic control and management," *IEEE Trans. Intell. Transp. Syst.*, vol. 21, no. 10, pp. 4063–4071, Oct. 2019.
- [6] F. Tao, Y. Zuo, L. Da Xu, and L. Zhang, "IoT-based intelligent perception and access of manufacturing resource toward cloud manufacturing," *IEEE Trans. Ind. Informat.*, vol. 10, no. 2, pp. 1547–1557, May 2014.
- [7] C. Xu, L. Yang, and P. Zhang, "Practical backscatter communication systems for battery-free Internet of Things: A tutorial and survey of recent research," *IEEE Signal Process. Mag.*, vol. 35, no. 5, pp. 16–27, Sep. 2018.
- [8] S. J. Thomas and M. S. Reynolds, "A 96 Mbit/sec, 15.5 pJ/bit 16-QAM modulator for UHF backscatter communication," in *Proc. IEEE Int. Conf. RFID (RFID)*, Orlando, FL, USA, 2012, pp. 185–190.
- [9] A. Shirane et al., "RF-powered transceiver with an energy- and spectral-efficient IF-based quadrature backscattering transmitter," *IEEE J. Solid-State Circuits*, vol. 50, no. 12, pp. 2975–2987, Dec. 2015.
- [10] S. J. Thomas, E. Wheeler, J. Teizer, and M. S. Reynolds, "Quadrature amplitude modulated backscatter in passive and semipassive UHF RFID systems," *IEEE Trans. Microw. Theory Techn.*, vol. 60, no. 4, pp. 1175–1182, Apr. 2012.
- [11] J. Kimionis, A. Georgiadis, S. N. Daskalakis, and M. M. Tentzeris, "A printed millimetre-wave modulator and antenna array for backscatter communications at gigabit data rates," *Nat. Electron.*, vol. 4, no. 6, pp. 439–446, 2021.
- [12] R. Correia and N. B. Carvalho, "Ultrafast backscatter modulator with low-power consumption and wireless power transmission capabilities," *IEEE Microw. Wireless Compon. Lett.*, vol. 27, no. 12, pp. 1152–1154, Dec. 2017.

- [13] R. Correia, A. Boaventura, and N. B. Carvalho, "Quadrature amplitude backscatter modulator for passive wireless sensors in IoT applications," *IEEE Trans. Microw. Theory Techn.*, vol. 65, no. 4, pp. 1103–1110, Apr. 2017.
- [14] J. Kimionis and M. M. Tentzeris, "Pulse shaping: The missing piece of backscatter radio and RFID," *IEEE Trans. Microw. Theory Techn.*, vol. 64, no. 12, pp. 4774–4788, Dec. 2016.
- [15] M. Biguesh and A. B. Gershman, "Training-based MIMO channel estimation: A study of estimator tradeoffs and optimal training signals," *IEEE Trans. Signal Process.*, vol. 54, no. 3, pp. 884–893, Mar. 2006.
- [16] C. He, Z. J. Wang, C. Miao, and V. C. M. Leung, "Block-level unitary query: Enabling orthogonal-like space-time code with query diversity for MIMO backscatter RFID," *IEEE Trans. Commun.*, vol. 15, no. 3, pp. 1937–1949, Mar. 2016.
- [17] C. He, S. Chen, H. Luan, X. Chen, and Z. J. Wang, "Monostatic MIMO backscatter communications," *IEEE J. Sel. Areas Commun.*, vol. 38, no. 8, pp. 1896–1909, Aug. 2020.
- [18] J. D. Griffin and G. D. Durgin, "Gains for RF tags using multiple antennas," *IEEE Trans. Antennas Propag.*, vol. 56, no. 2, pp. 563–570, Feb. 2008.
- [19] C. He and Z. J. Wang, "Closed-form BER analysis of non-coherent FSK in MISO double rayleigh fading/RFID channel," *IEEE Commun. Lett.*, vol. 15, no. 8, pp. 848–850, Aug. 2011.
- [20] C. Boyer and S. Roy, "Space time coding for backscatter RFID," *IEEE Trans. Wireless Commun.*, vol. 12, no. 5, pp. 2272–2280, May 2013.
- [21] C. He, H. Luan, X. Li, C. Ma, L. Han, and Z. J. Wang, "A simple, high-performance space-time code for MIMO backscatter communications," *IEEE Internet Things J.*, vol. 7, no. 4, pp. 3586–3591, Apr. 2020.
- [22] M. Asif, A. Ihsan, W. U. Khan, A. Ranjha, S. Zhang, and S. X. Wu, "Energy-efficient beamforming and resource optimization for AmbSC-assisted cooperative NOMA IoT networks," *IEEE Internet Things J.*, vol. 10, no. 14, pp. 12434–12448, Jul. 2023.
- [23] M. Ahmed et al., "Cooperative backscatter NOMA with imperfect SIC: Towards energy efficient sum rate maximization in sustainable 6G networks," *J. King Saud Univ.-Comput. Informat. Sci.*, vol. 34, no. 10, pp. 7940–7947, 2022.
- [24] M. Asif, A. Ihsan, W. U. Khan, A. Ranjha, S. Zhang, and S. X. Wu, "Energy-efficient backscatter-assisted coded cooperative NOMA for B5G wireless communications," *IEEE Trans. Green Commun. Netw.*, vol. 7, no. 1, pp. 70–83, Mar. 2023.
- [25] M. Jin, Y. He, C. Jiang, and Y. Liu, "Parallel backscatter: Channel estimation and beyond," *IEEE/ACM Trans. Netw.*, vol. 29, no. 3, pp. 1128–1140, Jun. 2021.
- [26] J. Ou, M. Li, and Y. Zheng, "Come and be served: Parallel decoding for COTS RFID tags," in *Proc. Annu. Int. Conf. Mobile Comput. Netw.*, 2015, pp. 500–511.
- [27] M. Jin, Y. He, X. Meng, Y. Zheng, D. Fang, and X. Chen, "FlipTracer: Practical parallel decoding for backscatter communication," in *Proc. ACM MobiCom*, 2017, pp. 275–287.
- [28] A. P. Sample, D. J. Yeager, P. S. Powledge, and J. R. Smith, "Design of a passively-powered, programmable sensing platform for UHF RFID systems," in *Proc. IEEE Int. Conf. RFID*, 2007, pp. 149–156.
- [29] J. D. Griffin, "High-frequency modulated-backscatter communication using multiple antennas," Ph.D. dissertation, School Electr. Comput. Eng., Georgia Inst. Technol., Atlanta, GA, USA, 2009.
- [30] J. D. Griffin and G. D. Durgin, "Multipath fading measurements at 5.8 GHz for backscatter tags with multiple antennas," *IEEE Trans. Antennas Propag.*, vol. 58, no. 11, pp. 3693–3700, Nov. 2010.
- [31] "RF-35: High volume commercial microwave and RF laminate." Taconic. [Online]. Available: <http://www.taconic.co.kr/download/RF-35.pdf>
- [32] H. Jeong and S. Kim, "Transistor-based modulator modeling technique using transfer learning for backscattered communication applications," in *Proc. IEEE Int. Microw. Symp.*, 2023, pp. 93–96.
- [33] G. Serpen and Z. Gao, "Complexity analysis of multilayer perceptron neural network embedded into a wireless sensor network," *Procedia Comput. Sci.*, vol. 36, pp. 192–197, 2014.
- [34] H. Jeong, D. Kim, G. Kim, and S. Kim, "VitRad: A low-cost continuous wave doppler radar system with 3D-printed horn antennas for human vital sign detection," *HardwareX*, vol. 12, Sep. 2022, Art. no. e00361.
- [35] H. Jeong and S. Kim, "Educational low-cost C-band FMCW radar system comprising commercial off-the-shelf components for indoor through-wall object detection," *Electronics*, vol. 10, no. 22, p. 2758, 2021.
- [36] K. Zhang, R. Tan, Z. H. Jiang, Y. Huang, L. Tang, and W. Hong, "A compact, Ultrawideband dual-Polarized Vivaldi antenna with radar cross section reduction," *IEEE Antennas Wireless Propag. Lett.*, vol. 21, pp. 1323–1327, 2022.
- [37] C. A. Balanis, *Advanced Engineering Electromagnetics*. Hoboken, NJ, USA: Wiley, 2012.
- [38] Z. Szabo, G.-H. Park, R. Hedge, and E.-P. Li, "A unique extraction of metamaterial parameters based on Kramers–Kronig relationship," *IEEE Trans. Microw. Theory Techn.*, vol. 58, no. 10, pp. 2646–2653, Oct. 2010.
- [39] O. Yesilyurt and G. Turhan-Sayan, "Metasurface lens for ultra-wideband planar antenna," *IEEE Antennas Wireless Propag. Lett.*, vol. 68, pp. 719–726, 2019.
- [40] S. Zhu, H. Liu, and P. Wen, "A new method for achieving miniaturization and gain enhancement of Vivaldi antenna array based on anisotropic metasurface," *IEEE Trans. Antennas Propag.*, vol. 67, no. 3, pp. 1952–1956, Mar. 2019.
- [41] A. R. H. Alhawari, A. Ismail, M. A. Mahdi, and R. S. A. R. Abdullah, "Antipodal Vivaldi antenna performance booster exploiting snug-in negative index metamaterial," *Prog. Electromagn. Res. C*, vol. 27, pp. 265–279, Mar. 2012.



Hyunmin Jeong received the B.S. degree in electronics engineering from Pusan National University, Busan, South Korea, in 2022, where he is currently pursuing the M.S. degree.

His current research interests include RF system, machine learning assisted backscattering communication, and antenna design.



Nohgyeom Ha received the B.S. and M.S. degrees in electronics engineering from Pusan National University, Busan, South Korea, in 2019 and 2022, respectively, where he is currently pursuing the Ph.D. degree in electronics engineering.

His current research interests include electromagnetic wave absorber design and mmWave-folded antenna.



Apostolos Georgiadis (Fellow, IEEE) was born in Thessaloniki, Greece. He received the B.S. degree in physics and the M.S. degree in telecommunications from Aristotle University of Thessaloniki, Thessaloniki, Greece, in 1993 and 1996, respectively, and the Ph.D. degree in electrical engineering from the University of Massachusetts at Amherst, Amherst, MA, USA, in 2002.

In 2002, he was a Systems Engineer with Global Communications Devices, North Andover, MA, USA, and worked on CMOS transceivers for wire-

less network applications. In June 2003, he was an RF/Analog Systems Architect with Bermat, Inc., Minnetonka, MN, USA. In 2005, he was a Juan de la Cierva Fellow with the University of Cantabria, Santander, Spain. In March 2007, he was a Senior Research Associate of Communications Subsystems with CTTC, Barcelona, Spain, where he was a Group Leader with the Microwave Systems and Nanotechnology Department from 2013 to 2016. In July 2016, he was an Associate Professor with Heriot-Watt University, Edinburgh, U.K. Since 2017, he has been with the European Patent Office, The Hague, The Netherlands. He has published more than 200 articles in peer reviewed journals and international conferences. His research interests include energy harvesting and wireless power transmission, radio frequency identification (RFID) technology, active antennas and phased array antennas, inkjet and 3-D printed electronics, and millimeter-wave systems.

Dr. Georgiadis was a recipient of the 2016 Bell Labs Prize (Third Place). He was the General Chair of 2011 IEEE RFID-TA Conference and the General Co-Chair of the 2011 IEEE MTT-S IMWS on Millimeter Wave Integration Technologies. He was the Chair of URSI Commission D: Electronics and Photonics. He has been an Associate Editor for the IEEE JOURNAL ON RADIO FREQUENCY IDENTIFICATION, the IEEE MICROWAVE AND WIRELESS COMPONENTS LETTERS, the *IET Microwaves Antennas and Propagation*, and the IEEE RADIO FREQUENCY IDENTIFICATION VIRTUAL JOURNAL. He co-founded and was an Editor-in-Chief of *Wireless Power Transfer* Journal (Cambridge). He has been a Distinguished Lecturer of IEEE CRFID. He is an EU Marie Curie Global Fellow and a URSI Fellow.



Manos M. Tentzeris (Fellow, IEEE) received the Diploma degree (magna cum laude) in electrical and computer engineering from the National Technical University of Athens, Athens, Greece, in 1987, and the M.S. and Ph.D. degrees in electrical engineering and computer science from the University of Michigan, Ann Arbor, MI, USA, in 1993 and 1998, respectively.

He is currently the Ken Byers Professor of Flexible Electronics with the School of Electrical and Computer Engineering, Georgia Institute of Technology, Atlanta, GA, USA, where he heads the ATHENA Research Group (20 Researchers). He has helped to develop academic programs in 3-D/inkjet-printed RF electronics and modules, flexible electronics, origami and morphing electromagnetics, highly integrated/multilayer packaging for RF, millimeter-wave, sub-THz, and wireless applications using ceramic and organic flexible materials, paper-based RFID's and sensors, wireless sensors and biosensors, wearable electronics, green electronics, energy harvesting and wireless power transfer, nanotechnology applications in RF, microwave MEMs, and System-on-Package-integrated (UWB, multiband, mmW, and conformal) antennas. He has authored more than 850 papers in refereed journals and conference proceedings, seven books, and 26 book chapters. He was a Visiting Professor with the Technical University of Munich, Munich, Germany, in 2002, with GTRI-Ireland, Athlone, Ireland, in 2009, and with LAAS-CNRS, Toulouse, France, in 2010.

Dr. Tentzeris was a recipient/co-recipient of the 2022 Georgia Tech Outstanding Doctoral Thesis Advisor Award, the 2019 Humboldt Research Prize, the 2017 Georgia Institute of Technology Outstanding Achievement in Research Program Development Award, the 2016 Bell Labs Award Competition Third Prize, the 2015 *IET Microwaves, Antennas, and Propagation* Premium Award, the 2014 Georgia Institute of Technology ECE Distinguished Faculty Achievement Award, the 2014 IEEE RFID-TA Best Student Paper Award, the 2013 *IET Microwaves, Antennas and Propagation* Premium Award, the 2012 FiDiPro Award in Finland, the iCMG Architecture Award of Excellence, the 2010 IEEE ANTENNAS AND PROPAGATION Society Piergiorgio L. E. Uslenghi Letters Prize Paper Award, the 2011 International Workshop on Structural Health Monitoring Best Student Paper Award, the 2010 Georgia Institute of Technology Senior Faculty Outstanding Undergraduate Research Mentor Award, the 2009 IEEE TRANSACTIONS ON COMPONENTS AND PACKAGING TECHNOLOGIES Best Paper Award, the 2009 E. T. S. Walton Award from the Irish Science Foundation, the 2007 IEEE AP-S Symposium Best Student Paper Award, the 2007 IEEE MTT-S IMS Third Best Student Paper Award, the 2007 ISAP 2007 Poster Presentation Award, the 2006 IEEE MTT-S Outstanding Young Engineer Award, the 2006 Asia-Pacific Microwave Conference Award, the 2004 IEEE TRANSACTIONS ON ADVANCED PACKAGING Commendable Paper Award, the 2003 NASA Godfrey Art Anzic Collaborative Distinguished Publication Award, the 2003 IBC International Educator of the Year Award, the 2003 IEEE CPMT Outstanding Young Engineer Award, the 2002 International Conference on Microwave and Millimeter-Wave Technology Best Paper Award (Beijing, China), the 2002 Georgia Institute of Technology-ECE Outstanding Junior Faculty Award, the 2001 ACES Conference Best Paper Award, the 2000 NSF CAREER Award, and the 1997 Best Paper Award of the International Hybrid Microelectronics and Packaging Society. He has served as the Head of the GTECE Electromagnetics Technical Interest Group, as the Georgia Electronic Design Center Associate Director of RFID/Sensors Research, as the Georgia Institute of Technology NSF-Packaging Research Center Associate Director of RF Research, and as the RF Alliance Leader. He was the TPC Chair of the IEEE MTT-S IMS 2008 Symposium and the Chair of the 2005 IEEE CEM-TD Workshop. He is the Vice-Chair of the RF Technical Committee (TC16) of the IEEE CPMT Society. He is the Founder and the Chair of the RFID Technical Committee (TC24) of the IEEE MTT-S and the Secretary/Treasurer of the IEEE C-RFID. He is an Associate Editor of the IEEE TRANSACTIONS ON MICROWAVE THEORY AND TECHNIQUES, the IEEE TRANSACTIONS ON ADVANCED PACKAGING, and the *International Journal on Antennas and Propagation*. He has given more than 100 invited talks to various universities and companies all over the world. He served as one of the IEEE MTT-S Distinguished Microwave Lecturers from 2010 to 2012 and is one of the IEEE CRFID Distinguished Lecturers. He is a member of the URSI-Commission D and the MTT-15 Committee, an Associate Member of EuMA, a Fellow of the Electromagnetic Academy, and a member of the Technical Chamber of Greece.



Sangkil Kim (Senior Member, IEEE) received the B.S. degree (magna cum laude) from the School of Electrical and Electronics Engineering, Yonsei University, Seoul, Republic of Korea, in 2010, and the M.S. and Ph.D. degrees from the School of Electrical and Computer Engineering, Georgia Institute of Technology, Atlanta, GA, USA, in 2012 and 2014, respectively.

From 2015 to 2018, he was a Senior Engineer with Qualcomm Inc., San Diego, CA, USA. He was with the Faculty of Department of Electronics Engineering, Pusan National University, Busan, Republic of Korea, in 2018. He has published 44 papers in peer reviewed journals and five book chapters. His main research interests are mmWave phased antenna array, machine learning assisted backscattering communication, RF biosensors, energy harvesting, and printed RF electronics.

Dr. Kim received the IET Premium Award Microwave, Antennas and Propagation in 2015 and the KIEES Young Researcher Award in 2019. He is a member of the IEEE MTT-26 RFID, *Wireless Sensors*, and IoT Committee.